

## Article

# Piece-Wise Droop Controller for Enhanced Stability in DC-Microgrid-Based Electric Vehicle Fast Charging Station

Mallareddy Mounica <sup>1</sup>, Bhooshan A. Rajpathak <sup>1</sup>, Mohan Lal Kolhe <sup>2,\*</sup>, K. Raghavendra Naik <sup>3</sup>,  
Janardhan Rao Moparthy <sup>4</sup> and Sravan Kumar Kotha <sup>1</sup>

<sup>1</sup> Electrical Engineering Department, Visvesvaraya National Institute of Technology, Nagpur 440010, India; mounicam7@gmail.com (M.M.); bhooshanar@eee.vnit.ac.in (B.A.R.); sravankumar.ee@gmail.com (S.K.K.)

<sup>2</sup> Faculty of Engineering and Science, University of Agder, 4604 Kristiansand, Norway

<sup>3</sup> AAU Energy Department, Aalborg University, 9220 Aalborg, Denmark; krna@energy.aau.dk

<sup>4</sup> Department of Electrical Engineering, Indian Institute of Technology, Dhanbad 826004, India; mjr.rao@gmail.com

\* Correspondence: mohan.l.kolhe@uia.no

**Abstract:** The need for public fast electric vehicle charging station (FEVCS) infrastructure is growing to meet the zero-emission goals of the transportation sector. However, the large charging demand of the EV fleet may adversely impact the grid's stability and reliability. To improve grid stability and reliability, the development of a DC microgrid (MG) leveraging renewable energy sources to supply the energy demands of FEVCSs is the sustainable solution. Balancing the intermittent EV charging demand and fluctuating renewable energy generation with the stable DC bus voltage of a DC MG is a challenging objective. To address this objective, a piece-wise droop control strategy is proposed in this work. The proposed scheme regulates DC bus voltage and power sharing with droop value updating in a region-based load current distribution. Voltage compensation in individual regions is carried out to further improve the degree of freedom. In this paper, the performance of the proposed strategy is evaluated with the consideration of real-time solar PV dynamics and EV load dynamics. Further, to showcase the effectiveness of the proposed strategy, a comparative analysis with a maximum power point tracking (MPPT) controller against various dynamic EV load scenarios is carried out, and the results are validated through a hardware-in-loop experimental setup. Despite the intermittent source and EV load dynamics, the proposed piece-wise droop control can maintain voltage regulation with less than 1% deviation.

**Keywords:** piece-wise droop control; DC fast charging station; DC fast charger; electric vehicle; energy storage unit; power sharing; bus voltage regulation; DC microgrid; solar PV; OPAL-RT



**Citation:** Mounica, M.; Rajpathak, B.A.; Kolhe, M.L.; Naik, K.R.; Moparthy, J.R.; Kotha, S.K. Piece-Wise Droop Controller for Enhanced Stability in DC-Microgrid-Based Electric Vehicle Fast Charging Station. *Processes* **2024**, *12*, 892. <https://doi.org/10.3390/pr12050892>

Academic Editor: Takuya Oda

Received: 19 March 2024

Revised: 17 April 2024

Accepted: 25 April 2024

Published: 28 April 2024



**Copyright:** © 2024 by the authors. Licensee MDPI, Basel, Switzerland. This article is an open access article distributed under the terms and conditions of the Creative Commons Attribution (CC BY) license (<https://creativecommons.org/licenses/by/4.0/>).

## 1. Introduction

Transitioning from traditional combustion vehicles to electric vehicles (EVs) stands out as the most effective strategy for curbing greenhouse gases and carbon emissions [1]. EVs are four to five times more efficient than internal combustion engines [2]. Additionally, the considerably good driving range and rapid charging feasibility of EV batteries with the availability of chargers between 25–150 kW have led to a rapid increase in EV adoption worldwide. To supply such a rapid increase in EV charging demand, compatible EV charging infrastructure is necessary. In countries like India, it is projected that by 2030, India may need 205 lakh charging stations to meet the future EV demand [3]. However, this transition presents a significant hurdle: a swift escalation in electricity consumption [4].

The stochastic nature of EV charging, coupled with the random arrival of vehicles at charging stations, poses a threat to utility grid stability and reliability [5]. This is because fast charging stations draw high currents for short durations to charge the EVs to the desired state of charge. Fast charging with pulse load characteristics causes peak loads

on the utility grid. Under scenarios of limited power supply during peak load conditions, the voltage at the DC bus fluctuates and may exceed the nominal value against the designed considerations of a 5–10% limit [6,7]. Additionally, overloading issues during peak loads can result in transformer heating and harmonic distortions [8]. The fluctuating voltage at the DC bus may result in unreliable fast charging and voltage stability issues [9]. To address the stochastic nature of EV charging events at fast charging stations, a DC microgrid configuration is proposed in this work. With DC microgrids [10], the detrimental impact of pulse-natured EV charging loads on grid stability and reliability can be significantly improved.

In situations where renewable energy and the grid are unavailable, the inclusion of an energy storage unit (ESU) guarantees an uninterrupted power supply to the load. In particular, compared to AC systems, a DC microgrid is advantageous for EV applications due to fewer conversion stages and losses. Also, the absence of reactive power and frequency, synchronizing tasks between the grid and other renewable sources can be omitted. Among all renewable sources, the photovoltaic system is the most effective and economical technology [11,12]. However, there are challenges with the intermittent nature of solar insolation; hence, the presence of an energy storage unit to maintain reliability is advisable [13,14].

In the integration of the dynamic fast charging station load with the time-varying irradiance of a solar PV into the DC microgrid, there can be a power imbalance issue with fluctuating voltage at the DC bus of the MG. To ensure power balance among various sources integrated into the DC microgrid, a robust controller is essential. Effective control of the microgrid-based charging station is paramount to attaining a stable supply to the dynamic load. Droop control is one such decentralized primary control technique that is robust and not complex [15–19]. The bus parameters of a DC microgrid such as bus voltage and power sharing can be controlled locally without any need for communication, but with a limitation of the trade-off between voltage regulation and current sharing. With proper current sharing, the load is equally distributed to all the parallel sources depending on their rating.

To partially mitigate the drawback of the traditional droop controller, certain controllers like the adaptive droop controller [20], multifunctional droop controller [21], and hybrid coordinated controller [22] are proposed in the literature, but the additional aid of a tertiary controller is needed to balance the trade-off between voltage regulation and power sharing of the DC microgrid. This requires additional communication infrastructure, which is not cost-effective, and the load on which these strategies are tested is not intermittent. The key research gaps identified from the literature are listed below.

- The limitation of basic droop control is not completely mitigated without additional support.
- The dynamic performance of the charging station with both an intermittent source and load is not studied.
- The charging station performance under a sudden load change of a large part of the load is not presented.
- A focused case study analyzing the impact of intermittent EV load dynamics on MG stability is partially explored.

Considering the stochastic EV charging dynamics and solar PV dynamics, Naik and Mohan [23,24] proposed prediction-based supervisory control strategies. These strategies enhanced the reliability and stability of DC microgrids with economically sized battery storage. In line with the contributions in [23,24], and in an extended effort to achieve enhanced reliability and stability of a DC MG considering fast charging station load against variable solar PV irradiance levels, a piece-wise droop control strategy is proposed in this research work.

The proposed piece-wise droop control technique establishes three regions [25–29] for the considered DC microgrid with DC fast charging station load. Three DC fast chargers are integrated with a solar PV and an ESU such that when each charger is connected to an EV,

the load current falls into one region of the piece-wise droop curve. This primary controller can mitigate the trade-off in voltage regulation and power sharing among the parallel sources of microgrids without any additional circuitry. The droop value and reference voltage are updated in every region individually to minimize the limitation of traditional droop controllers. In this work, the DC microgrid model intends to supply a fast electric vehicle charging station comprised of a solar PV and an ESU, which are connected to a DC bus through DC–DC converters. All the fast chargers are rated at 62.5 kW high-power charging, representing the standards of the Indian EV market. The Matlab/Simulink environment is utilized to analyze the performance and stability of the charging station under dynamic source and load conditions during rapid and substantial load changes. The modeling results are validated using the OPLALRT real-time simulator experimental setup.

The following objectives are achieved with the proposed controller in this work:

- (i) voltage regulation and power balance improvement without any trade-off, unlike traditional controllers;
- (ii) low degree of communication between integrated sources, which makes the charging station ineffective from any communication failure;
- (iii) piece-wise droop controller with two degrees of freedom of control;
- (iv) stable charging station operation against real-time intermittent source and EV load dynamics;
- (v) investigation of the dynamics of charging stations under substantial fluctuations in EV load, incrementally varying by one-third of the total EV load;
- (vi) fast charging EVs up to 80% SOC within an hour with a real-time rapid charger.

Section 2 illustrates the configuration of a microgrid-based DC fast charging station. Section 3 focuses on the proposed piece-wise droop control. Section 4 presents the Modeling results and assessment followed by the Experimental Validation through RT lab in Section 5. Section 6 concludes the paper.

## 2. Proposed Microgrid-Based DC Fast Charging Station Configuration and Control

The proposed DC fast charging station model shown in Figure 1, comprises solar PV connected to a DC bus through a unidirectional DC–DC converter and ESU connected through a bidirectional DC–DC converter in the source side. The bus voltage is considered 750 V in this work, which is reasonable for the high-power rapid charging of EVs. The unidirectional converter steps up the voltage from the solar PV to 750 V at the output terminal of the converter. The proposed piece-wise droop controller is used to operate this converter to generate a stable bus voltage and proper current sharing between the solar PV and ESU for stable and reliable operation. The proposed controller updates the droop value based on the load demand and generates pulses to the converter accordingly such that a stable bus voltage is maintained. Perturb and Observe MPPT control is also implemented in this converter to compare the robustness of the proposed controller.

The bidirectional converter ensures the power flow from the PV to charge the ESU when the PV power is more than the load power. It discharges the ESU by supplying load whenever the PV power is insufficient for the total demand. The voltage–current loop control is implemented for the bidirectional converter. The load to the PV–ESU microgrid is a DC fast charging station with three real-time 62.5 kW rapid chargers of Indian standards. Each charger is connected through a DC fast charger and can charge one EV at a time. Each charger can charge the EV battery at 500 V and 125 A such that a high power of 62.5 kW is supplied to each EV, aiding in rapid charging. The detailed control of the converters is discussed in the following sub-sections. The one-sided arrow in red from the Figure 1 represents the uni-directional power flow and two-sided arrow represents the bi-directional power flow.

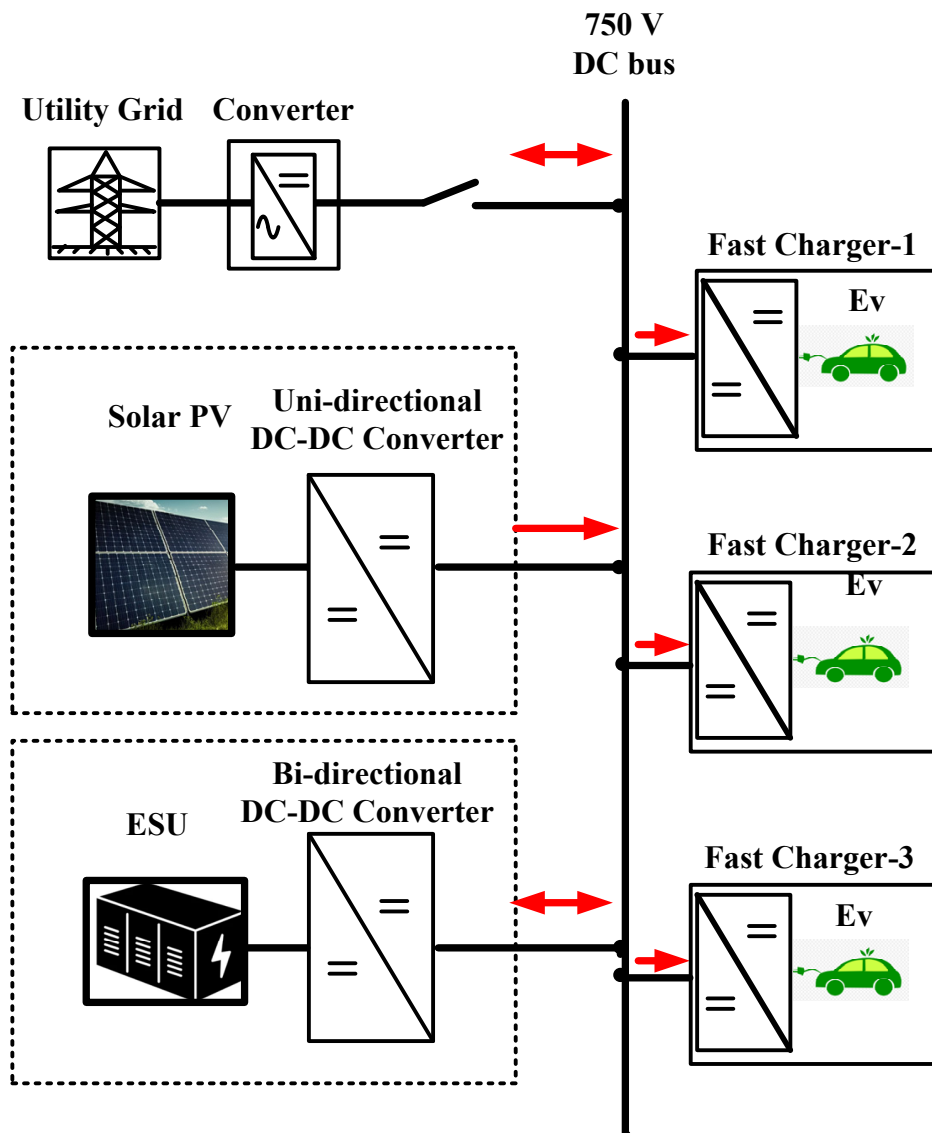


**Figure 1.** Schematic view of proposed microgrid-based DC fast charging station.

### 2.1. Control of Unidirectional and Bidirectional DC–DC Converter

The boost converter is used to integrate the solar PV with the DC bus through an input capacitor ( $C_{pv}$ ) as shown in Figure 2. It boosts the input voltage ( $V_{pv}$ ) to the desired level using an inductor ( $L_{pv}$ ). The proposed piece-wise droop controller for this converter consists of a cascaded voltage–current loop. The inner current loop generates the reference ( $I_{pv-ref}$ ) for the outer voltage loop. Droop updating and voltage compensation are integrated with the outer voltage loop. The signals are generated through a pulse width modulator (PWM) for the boost converter. The ESU is integrated with the DC bus through a bidirectional DC–DC converter, which can boost or buck the input voltage ( $V_{esu}$ ) according to the system operation. These arrows presents complementary pulses and it is self-explanatory form the figure.

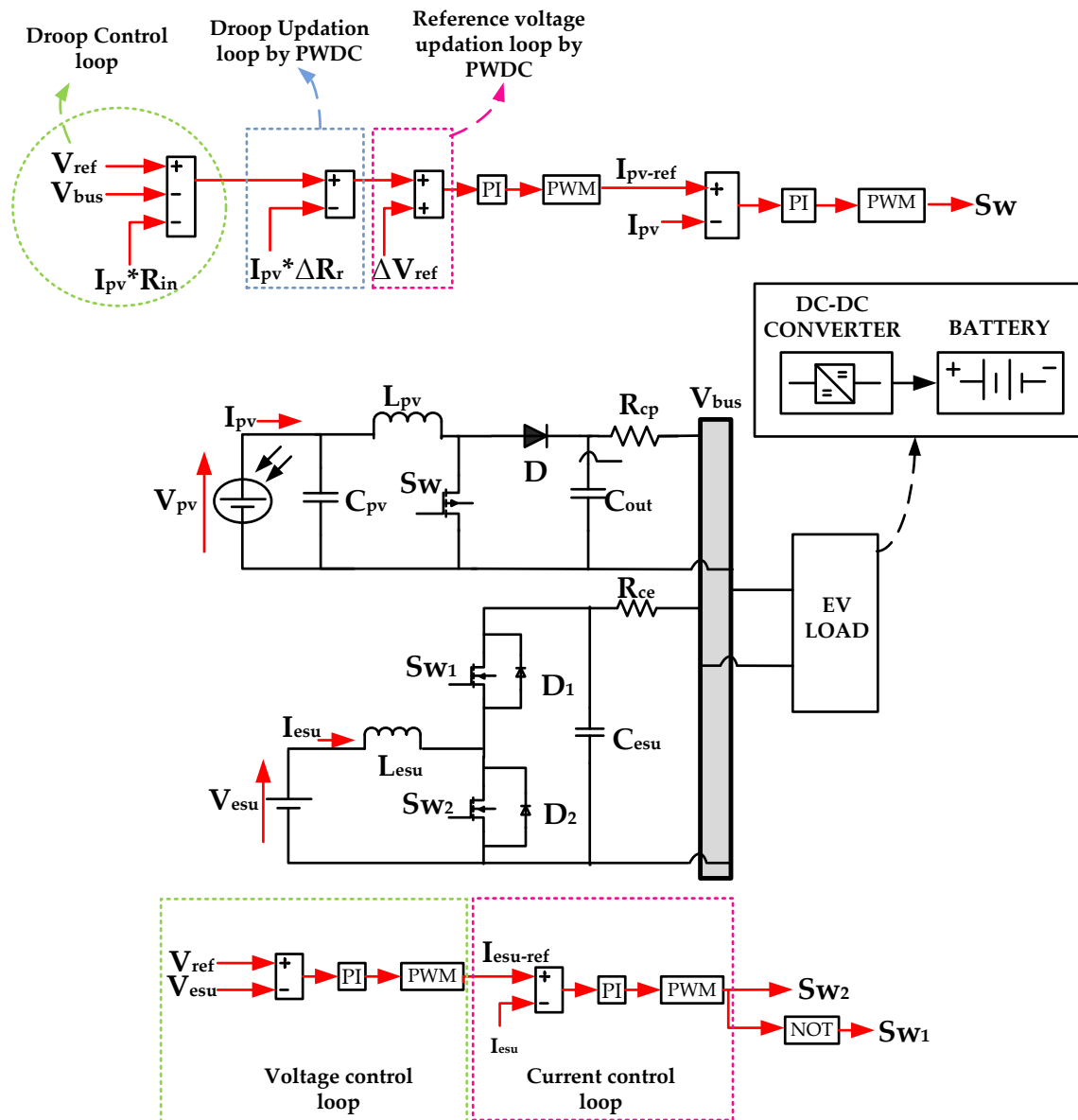


Figure 2. Control structure of solar PV and ESU.

When the solar power exceeds the total EV power, the excess energy is used to charge the ESU, and the DC–DC converter acts in buck mode. When the solar power is not enough to supply the load to the bus, the ESU discharges the energy through the converter acting in boost mode. The pulses are generated by the PWM through the voltage control loop. In Figure 2,  $C_{out}$  is the output capacitance of the boost converter,  $I_{pv}$  is the solar PV current,  $R_{cp}$  and  $R_{ce}$  are the cable resistance of unidirectional and bidirectional converters, respectively,  $V_{ref}$  is the reference voltage,  $V_{bus}$  is the DC bus voltage,  $I_{esu}$  is the input current of ESU,  $C_{esu}$  and  $L_{esu}$  are the capacitor and inductor of the bidirectional converter,  $\Delta V_{ref}$  is the change in voltage reference value in the voltage compensation loop, and  $R_{in}$  is the initial droop value.

### 2.2. DC Fast Charger

The DC fast charger shown in Figure 3 consists of a buck converter decreasing the DC bus voltage to the incoming EV voltage ( $V_{ev}$ ) requirements. A cascaded voltage–current loop is implemented to control the fast charger. The reference voltage and EV voltage are compared to generate an error signal in the voltage control loop, which is the primary control loop. This is passed through the PI controller to generate the reference current for

the secondary control loop, which is the current control loop. The pulses are generated by a PWM generator such that the rapid charger provides the rated voltage and current of 500 V and 125 A, respectively, to charge the incoming EV at the 62.5 kW power level. The real-time specification of a high-power DC fast charger of 62.5 kW is considered in this work. The reference voltage and current for the charger are listed in Appendix A, Table A1.

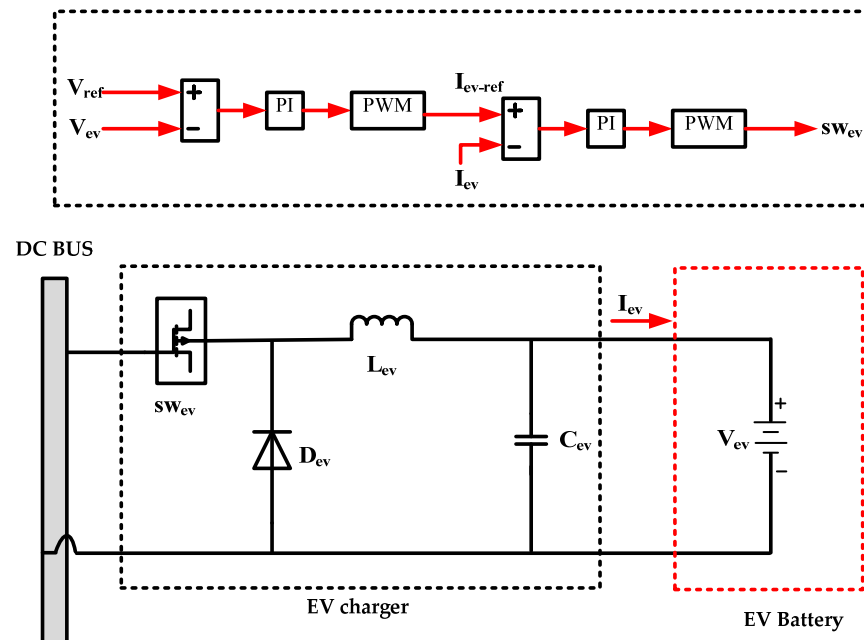


**Figure 3.** Control configuration of DC fast charger to charge the EV batteries.

$I_{ev}$  is the EV current,  $I_{ev-ref}$  is the reference current for the controller, and  $L_{ev}$  and  $C_{ev}$  are the inductor and capacitor of the DC fast charger.

The SOC is the state of charge of the battery, which indicates the capacity of the battery remaining compared to its full capacity. It is always advisable for EV consumers to maintain the battery SOC within safe limits. Deep discharge or overcharge of the battery may deplete its life span and affect the travel range of the EV. The specifications of the EV considered in this work are mentioned in Appendix A, Table A1.

### 3. Piece-Wise Droop Control along with Voltage Compensation

#### 3.1. Limitation of Traditional Droop Control

The output voltage of the unidirectional converter of the solar PV with cable resistance is as given by Equation (1).

$$V_{bus} = V_{ref} - I_{pv}(R_{in} + R_{cp}) \quad (1)$$

The linear droop resistance value can be estimated from the maximum allowable change in bus voltage ( $\Delta V_{max}$ ) and the maximum solar PV power. Practically, the droop resistance value is limited to the value satisfying Equation (2).

$$R_{in} \times I_{pv} = \Delta V_{max} \quad (2)$$

The bus voltage deviation and current sharing are the functions of load resistance ( $R_l$ ) and cable resistance of the parallel sources, i.e., the PV and ESU of the charging station, which is given by Equation (3) [29].

$$V_{bus} = \frac{R_l(R_{ce} + R_{in})V_{pv} + R_l(R_{cp} + R_{in})V_{esu}}{R_l(R_{cp} + R_{in}) + R_l(R_{ce} + R_{in}) + (R_{cp} + R_{in})(R_{ce} + R_{in})} \quad (3)$$

The current-sharing difference ( $\Delta I$ ) between the PV and ESU is given by Equation (4).

$$\Delta I = I_{pv} - I_{esu} = \frac{[R_l(V_{pv} - V_{esu}) + V_{pv}(R_{ce} + R_{in})] - [R_l(V_{esu} - V_{pv}) + V_{esu}(R_{cp} + R_{in})]}{R_l(R_{cp} + R_{in}) + R_l(R_{ce} + R_{in}) + (R_{cp} + R_{in})(R_{ce} + R_{in})} \quad (4)$$

From the above equations, the higher the droop resistance, the lower the bus voltage, and the better the current sharing. The lower the droop resistance, the higher the bus voltage, and the worse the current sharing. This means that there exists a trade-off between voltage regulation and current sharing throughout the operation with a predetermined droop value. To mitigate this, the droop resistance value should be updated according to the load condition. Under light load conditions, the source nearer to the load with less resistance supplies more power, which is advantageous, but it creates a lower-utility system in heavy load conditions. Hence, low droop resistance under light loads and high droop resistance under heavy load is preferable. Hence, the smaller the droop resistance, the better the voltage regulation, and the larger the current-sharing difference. The larger the droop resistance, the worse the voltage regulation, and the better the current sharing. With the proposed controller, the power sharing of the source with the higher resistance increases as the load increases.

### 3.2. Piece-Wise Droop Curve Construction

To overcome the limitation of the traditional droop control technique, the droop characteristics plot is divided into certain regions through the boundary current ( $I_r$ ), and the droop value is updated in every region. The droop value is small for the initial region, and it keeps increasing with the progression of the region. This increases the utilization of sources under both light and heavy loads, unlike the traditional controllers. The source near to the load shares more power than the other sources under the light load condition with a low droop value, whereas the high droop value under heavy load exhibits the better power sharing among all the sources, improving plant utilization under all circumstances. The constraints for the droop value in each region are the maximum allowable voltage and the current range for that particular region.

Apart from the droop coefficient, the reference voltage also impacts the bus voltage, which is inferred from Equation (1). Voltage can be compensated for by varying the reference voltage in each region, thereby aiding in better voltage regulation. The piece-wise droop curve having three regions with both droop updating and voltage compensation is depicted in Figure 4. The three regions of the proposed droop controller [26] are Region I ( $R_I$ ), Region II ( $R_{II}$ ), and Region III ( $R_{III}$ ). The voltage constraint for each region is given by Equation (5).

$$\Delta V_{max} = \sum_j^r \Delta V_j \quad (5)$$

where  $\Delta V_{max}$  is the maximum allowable variation in voltage, which is 5% of the nominal bus voltage, and  $j = 1 \dots r$  in which  $j = 1$  for Region II, and so on. The current constraint ( $I_{max}$ ) for each region is given by Equation (6).

$$I_{max} = \sum_j^r \Delta I_j \quad (6)$$

where  $I_{max}$  represents the maximum source current of that region. The estimated values of  $\Delta V_{max}$  and  $I_{max}$  are given in the following equations [25].

$$\delta V = a \times j \times \delta V_1 \quad (7)$$

$$\delta I = b \times (r + 1 - j) \times \delta I_r \quad (8)$$

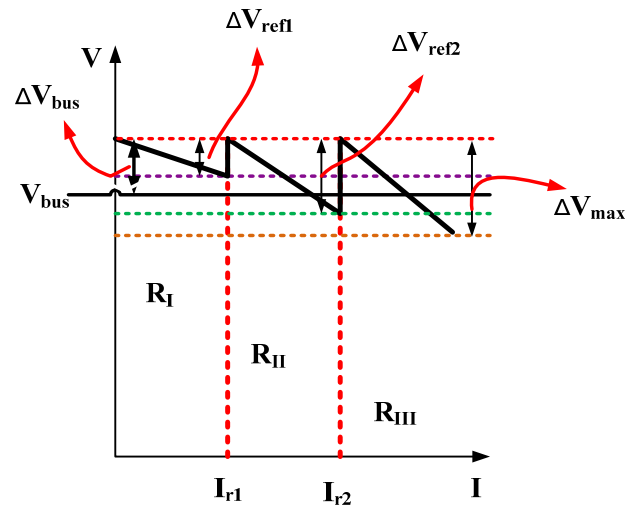


**Figure 4.** Piece-wise droop curve for three regions with voltage compensation.

$\delta V_1$  and  $\delta I_r$  are the variations in voltage range in  $R_I$  and the current range in  $R_{III}$ . Substituting Equations (7) and (8) into Equations (5) and (6) gives the values of  $\delta V_1$  and  $\delta I_r$  as follows.

$$\delta V_1 = \frac{\Delta V_{max}}{1 + a\left(\left(\frac{r}{2}(r+1)\right) - 1\right)} \quad (9)$$

$$\delta I_r = \frac{I_{max}}{1 + b\left(\left(\frac{r}{2}(r+1)\right) - 1\right)} \quad (10)$$

The droop coefficient for each region is given as follows.

$$d_r = \left(\frac{b}{a}\right) \left(\frac{j}{r+1-j}\right) \left(\frac{\delta V_1}{\delta I_r}\right) \quad (11)$$

The droop values calculated for all the regions are listed in Table 1 as follows.

**Table 1.** Droop coefficients for piece-wise droop curve.

| Control Strategy         | Region I      | Region II       | Region III      |
|--------------------------|---------------|-----------------|-----------------|
| MPPT                     | 0.05 $\Omega$ | NA              | NA              |
| Piece-wise droop control | 0.05 $\Omega$ | 0.0727 $\Omega$ | 0.2182 $\Omega$ |

NA—not applicable.

### 3.3. Bus Voltage and Current Sharing for Various Regions of the Droop Curve

In the proposed piece-wise droop controller, the droop curve is divided into three regions. Dividing the droop curve into more than three regions will provide minimal improvement in the system performance for the same load current distribution [29]. The governing equations as a function of droop resistance and reference voltage for various regions of the piece-wise droop curve are given as follows. Equation (12) indicates the bus voltage equation for  $R_I$ , Equation (13) for  $R_{II}$ , and Equation (14) for  $R_{III}$ , respectively, with droop updating.

$$V_{bus} = V_{ref} - I_{pv}(R_{in} + R_{cp}) \text{ for } I_{pv} < I_{r1} \quad (12)$$

$$V_{bus} = \left(V_{ref} + \Delta V_{ref1}\right) - I_{pv}(R_{in} + R_{cp} + p_1) + p_1(I_{r1}) \text{ for } I_{r1} < I_{pv} < I_{r2} \quad (13)$$

$$V_{bus} = \left(V_{ref} + \Delta V_{ref2}\right) - I_{pv}(R_{in} + R_{cp} + p_2) + p_2(I_{r2}) \text{ for } I_{pv} > I_{r2} \quad (14)$$

The constants  $p_1$  and  $p_2$  are the function of source voltage and resistance values as shown in Equations (15)–(17).

$$p_r = p_1 + p_2 \quad (15)$$

$$p_1 = V_{bus}(R_{cp} + R_{ce}) - I_r R_l R_{cp} R_{ce} - 2R_l \Delta V_{bus} / 2V_{bus} - 4I_r R_l \quad (16)$$

$$p_2 = \left( \frac{(I_e R_l - V_{bus})^2 (R_{cp}^2 + R_{ce}^2) + 4R_l^2 \Delta V_{bus}^2 - 2R_{cp} R_{ce} V_{bus}^2}{+4I_r R_l (R_{cp} R_{ce} V_{bus} - R_l (R_{cp} + R_{ce}) \Delta V_{bus})} \right)^{1/2} / 2V_{bus} - 4I_r R_l \quad (17)$$

The voltage compensation for the reference voltage in each region is given by Equation (18), and the updated reference value of each region is listed in Table 2.

$$\Delta V_{refr} = \left( 0.5 \times \sum_r I_{rr} \right) \times R_{in} \times r \quad (18)$$

where  $r = 1$  for  $R_{II}$  and  $r = 2$  for  $R_{III}$ . Figure 5 shows the flowchart of the various steps involved in updating the droop coefficient and voltage compensation in each region. The sample calculations are listed in Appendix B, Tables A2 and A3. After the droop updating and voltage compensation by the above equations, the current difference equation implying power sharing between the PV and ESU for  $R_{II}$  and  $R_{III}$  is given by Equations (19) and (20), respectively.

$$\Delta I = \frac{\alpha_{II} - \beta_{II}}{\gamma_{II}} \quad (19)$$

where

$$\Delta I = I_{pvII} - I_{esu}$$

$$\alpha_{II} = \left[ R_l (V_{pv} + \Delta V_{ref1} - V_{esu}) + (V_{pv} + \Delta V_{ref1})(R_{ce} + d_{pvII}) \right]$$

$$\beta_{II} = \left[ R_l (V_{esu} - V_{pv} + \Delta V_{ref1}) + V_{esu}(R_{cp} + d_{pvII}) \right]$$

$$\gamma_{II} = \left[ R_l (R_{cp} + d_{pvII}) + R_l (R_{ce} + d_{pvII}) + (R_{cp} + d_{pvII}) \times (R_{ce} + d_{pvII}) \right]$$

$$\Delta I = \frac{\alpha_{III} - \beta_{III}}{\gamma_{III}} \quad (20)$$

where

$$\Delta I = I_{pvIII} - I_{esu}$$

$$\alpha_{III} = \left[ R_l (V_{pv} + \Delta V_{ref1} - V_{esu}) + (V_{pv} + \Delta V_{ref1})(R_{ce} + d_{pvIII}) \right]$$

$$\beta_{III} = \left[ R_l (V_{esu} - V_{pv} + \Delta V_{ref1}) + V_{esu}(R_{cp} + d_{pvIII}) \right]$$

$$\gamma_{III} = \left[ R_l (R_{cp} + d_{pvIII}) + R_l (R_{ce} + d_{pvIII}) + (R_{cp} + d_{pvIII}) \times (R_{ce} + d_{pvIII}) \right]$$

**Table 2.** Voltage reference for piece-wise droop curve.

| Control Strategy         | Region I | Region II | Region III |
|--------------------------|----------|-----------|------------|
| MPPT                     | 750 V    | NA        | NA         |
| Piece-wise droop control | 750 V    | 761.25 V  | 772.5 V    |

NA—not applicable.

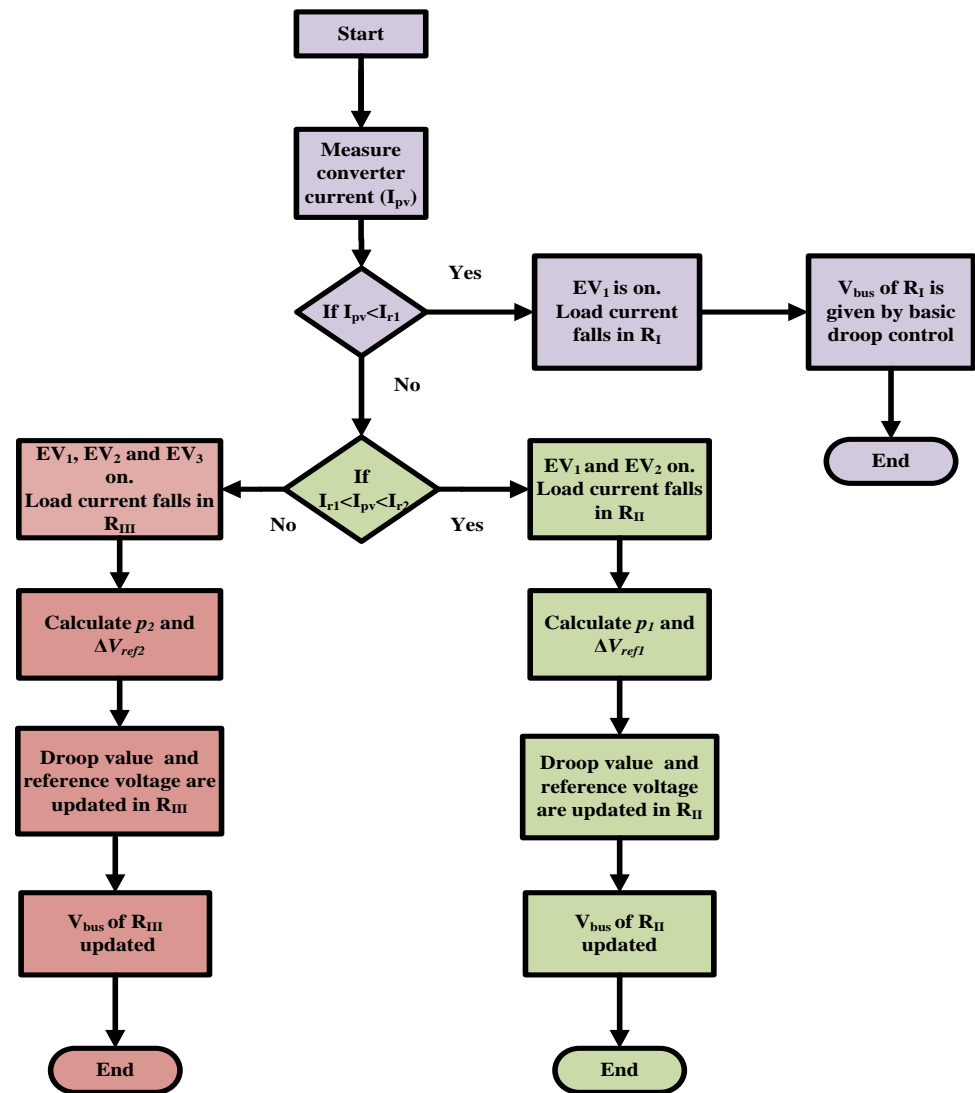


**Figure 5.** Flowchart of the proposed piece-wise droop control for three regions along with voltage compensation. Different colours represents different regions of the pice-wise droop curve.

#### 4. Simulation Assessment of FEVCS

The proposed microgrid-based DC fast charging station model is simulated with real-time variable solar irradiation at different load conditions to validate the efficacy of the proposed control algorithm. The real-time variable solar irradiation of the Nagpur region in India for 2022 is scaled down to 12 s and is plotted in Figure 6. The system parameters are listed in Appendix A, Table A1. The load on the DC bus consists of three EVs, for which EV<sub>1</sub> is in at t = 1 s to the charging station and out at t = 12 s. Likewise, EV<sub>2</sub> is in at t = 4 s and out at t = 12 s. EV<sub>3</sub> is in at t = 8 sec and out at t = 12 s. Based on the total EV power, the load current is divided into three regions.

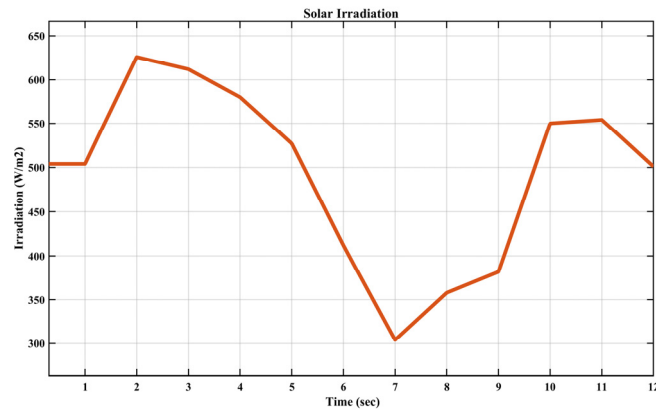


Figure 6. Solar irradiation.

The load profile of the EV charging station consists of operating conditions from no load to full load, which is represented by Table 3. From  $t = 0$  to  $t = 1$ , the charging station is under no load. From  $t = 1$  to  $t = 4$  s, the charging station is under one-third load. From  $t = 4$  to  $t = 8$  s, the charging station is under a two-thirds load. From  $t = 8$  to  $t = 12$  s, the charging station is under full load.

Table 3. Load profile of DC fast charging station.

| Time (s)        | 0 | 1 | 2              | 3 | 4 | 5 | 6               | 7 | 8 | 9 | 10               | 11 | 12 |
|-----------------|---|---|----------------|---|---|---|-----------------|---|---|---|------------------|----|----|
| EV <sub>1</sub> |   |   | R <sub>I</sub> |   |   |   |                 |   |   |   |                  |    |    |
| EV <sub>2</sub> |   |   |                |   |   |   | R <sub>II</sub> |   |   |   |                  |    |    |
| EV <sub>3</sub> |   |   |                |   |   |   |                 |   |   |   | R <sub>III</sub> |    |    |

The proposed DC fast charging station is simulated with the MPPT controller, which is widely used for solar PV control, and compared to the proposed controller.

#### 4.1. With MPPT

The Perturb and Observe MPPT technique is implemented for the unidirectional converter of the solar PV. The DC bus voltage ( $V_{bus}$ ) in Figure 7 has ripples beyond 5% of the nominal bus voltage.

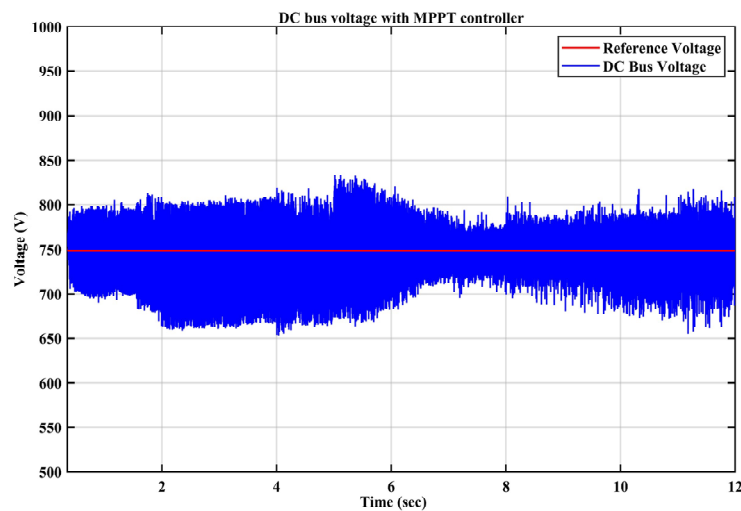


Figure 7. DC bus voltage with MPPT controller.

Figure 8 shows the voltage, current, and power output of the solar PV with an MPPT controller. The variation in current and power is due to the variable irradiation. Figure 9 represents the ESU voltage, current, and power. The rate of the SOC rise and fall in the ESU varies with variations in the solar PV output. Figure 10 represents the power-sharing plot of the solar, ESU and total EV power ( $P_{ev}$ ), which is the sum of the powers of EV<sub>1</sub>, EV<sub>2</sub>, and EV<sub>3</sub>. From  $t = 0$  to  $t = 1$  s, there is no load on the DC bus. Hence, the total power produced by the solar PV is utilized to charge the ESU. From  $t = 1$  to  $t = 4$  s, the load requirement is approximately 62.5 kW. The excess power from the solar PV after supplying the load is utilized to charge the ESU. At around  $t = 7$  s, the solar irradiation is very low and is sufficient to charge only the EV load on the bus; hence, the ESU is ideal without charging or discharging.

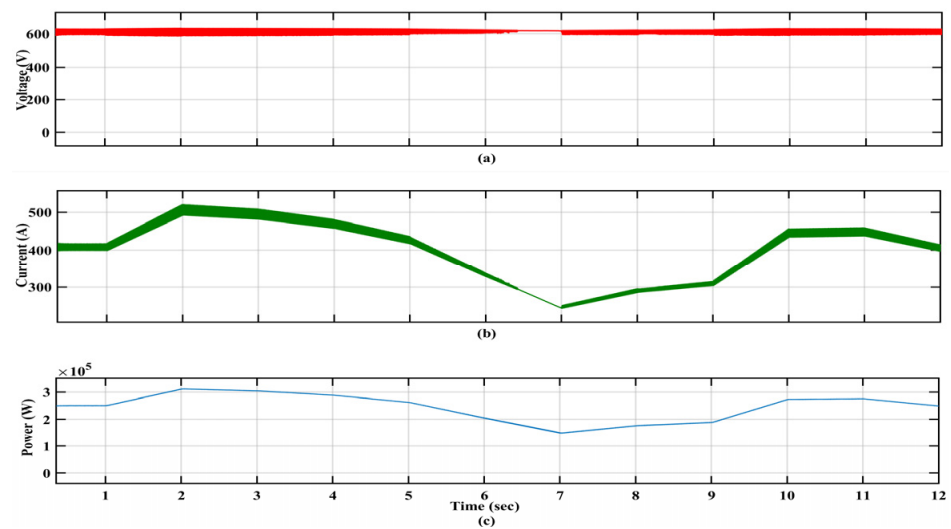


Figure 8. Solar PV (a) voltage, (b) current, and (c) power with MPPT controller.

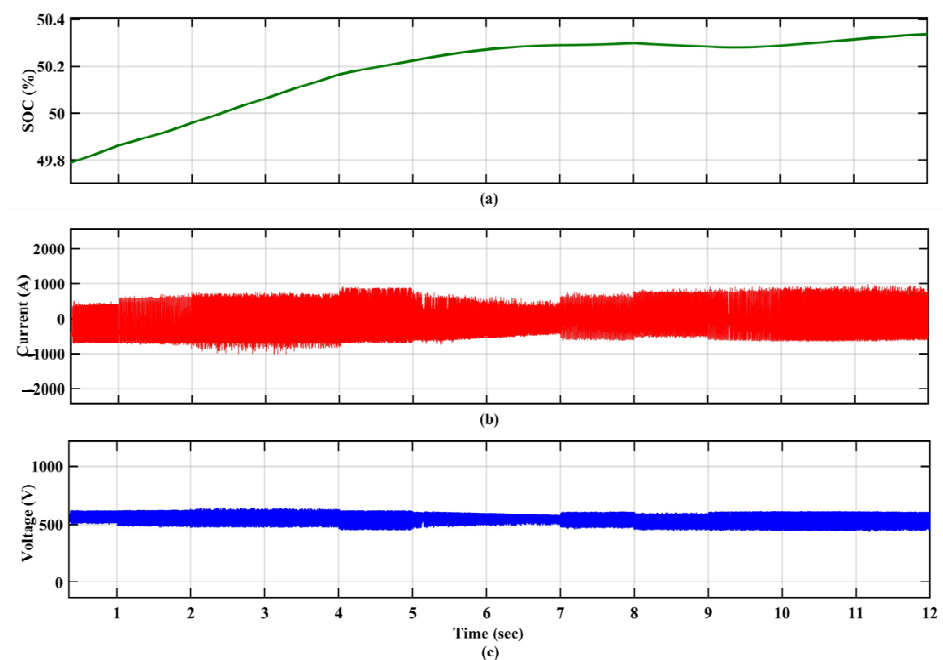


Figure 9. ESU (a) SOC, (b) current, and (c) voltage with MPPT controller.

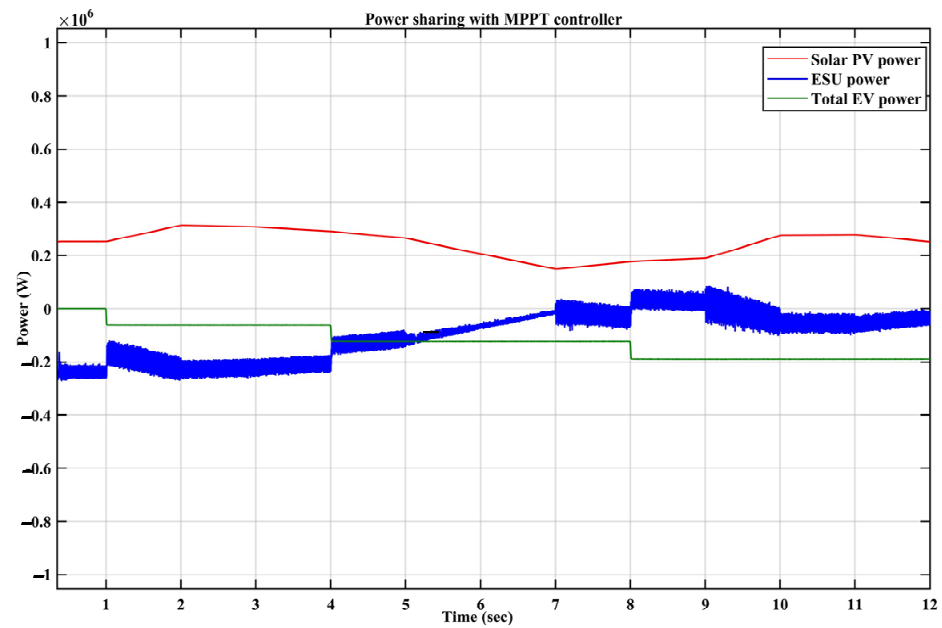


Figure 10. Power sharing with MPPT controller.

All the EVs are charged at 500 V and 125 A, which is the rated voltage and current of a fast DC charger. The initial voltage is 474.2 V for all the EVs, as shown in Figures 11a, 12a and 13a. All the EVs are charging at 125 A as shown in Figure 11b for EV<sub>1</sub>, Figure 12b for EV<sub>2</sub>, and Figure 13b for EV<sub>3</sub>. According to the EV rating considered in this work, the maximum voltage of the EV battery can reach 516 V if it is charged up to 100% SOC. However, it is always recommended to stop the fast charging when the SOC of the EV reaches 80%, after which slow charging is preferred.

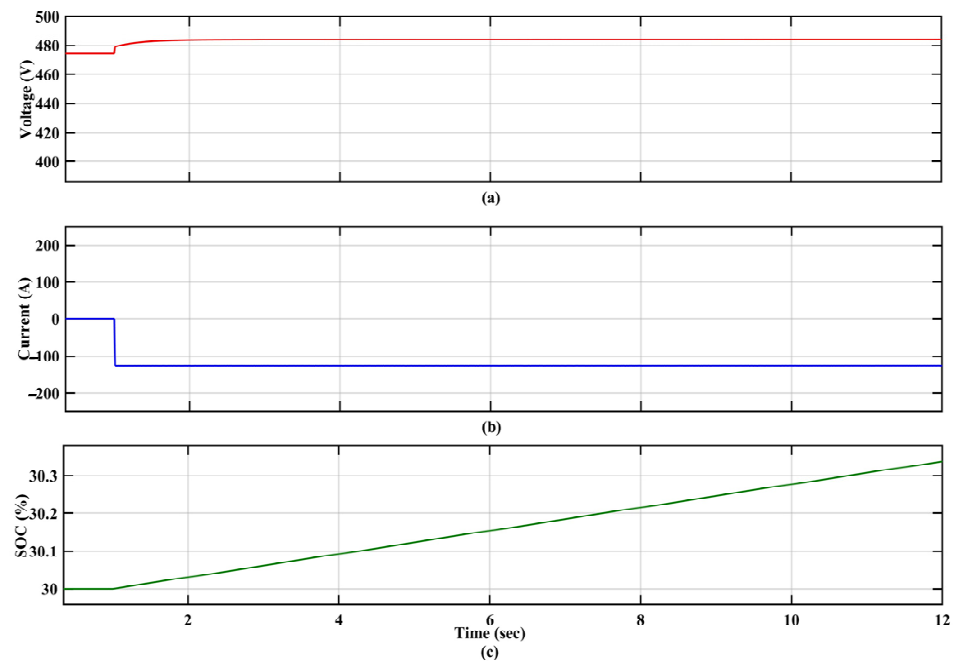


Figure 11. EV<sub>1</sub> (a) voltage, (b) current, and (c) SOC with MPPT controller.

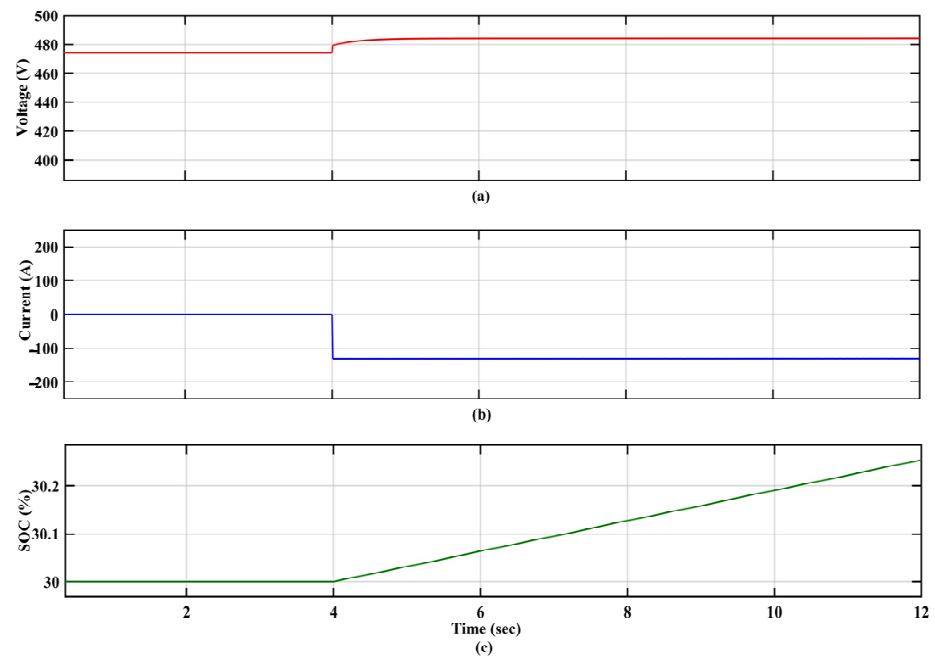


Figure 12. EV<sub>2</sub> (a) voltage, (b) current, and (c) SOC with MPPT controller.

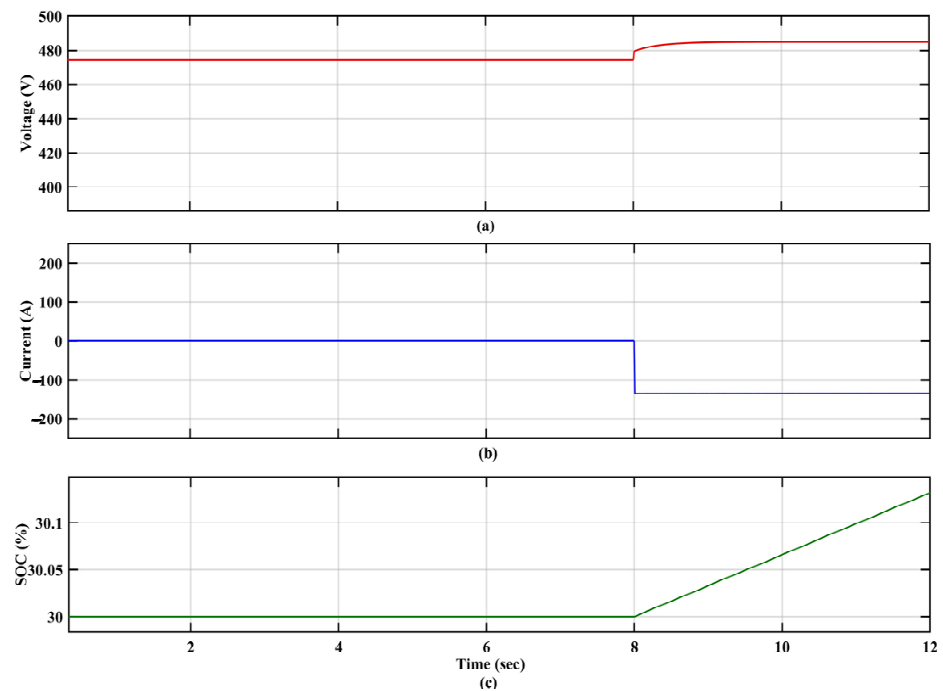


Figure 13. EV<sub>3</sub> (a) voltage, (b) current, and (c) SOC with MPPT controller.

The SOC of EV<sub>1</sub> starts rising from 30% from  $t = 1$  s to 30.34% until  $t = 12$  s, as shown in Figure 11c. The SOC of EV<sub>2</sub> rises from 30% at  $t = 4$  s to 30.25% until  $t = 12$  s, as shown in Figure 12c. The SOC of EV<sub>3</sub> rises from 30% at  $t = 8$  s to 30.13% until  $t = 12$  s, as shown in Figure 13c.

#### 4.2. With the Proposed Controller

The piece-wise droop curve is divided into three regions based on the load on the DC bus with two boundary currents. The boundary current of  $R_I$  and  $R_{II}$  is  $I_{r1} = 150$  A and the boundary current of  $R_{II}$  and  $R_{III}$  is  $I_{r2} = 300$  A.

#### 4.2.1. Region I ( $t = 1$ to $t = 4$ s)

When EV<sub>1</sub> is plugged into the charging station, the DC bus is under one-third load and the EV load current is 125 A, which is less than  $I_{r1}$  and falls into  $R_1$ . The droop value is the same as the initial droop value without any updating and no voltage compensation for this region, which means the performance of the charging station is the same as with the basic droop control.

Figure 14 represents  $V_{bus}$ , which is almost tracking the reference voltage without any ripple out of tolerable range in the instances of EVs being plugged in. There is an ignorable fluctuation in the bus voltage, which settles in almost less than 0.1 s when EV<sub>1</sub> is plugged in. The highest peak attained in this region is 754.34 V, and the voltage dips up to 744.36 V which is in the tolerable range of fluctuation for the bus voltage. Figure 15 shows  $V_{pv}$ ,  $I_{pv}$ , and  $P_{pv}$  of the solar PV. The solar input voltage is constant throughout the operation, irrespective of the variable irradiation, which shows the robustness of the proposed controller. The current and power are variable according to the variable irradiation of the solar PV. The ripples in the ESU current are minimized with the proposed controller when compared to the MPPT controller, which is evident from Figure 16, indicating the improved power balance with the proposed piece-wise droop controller.

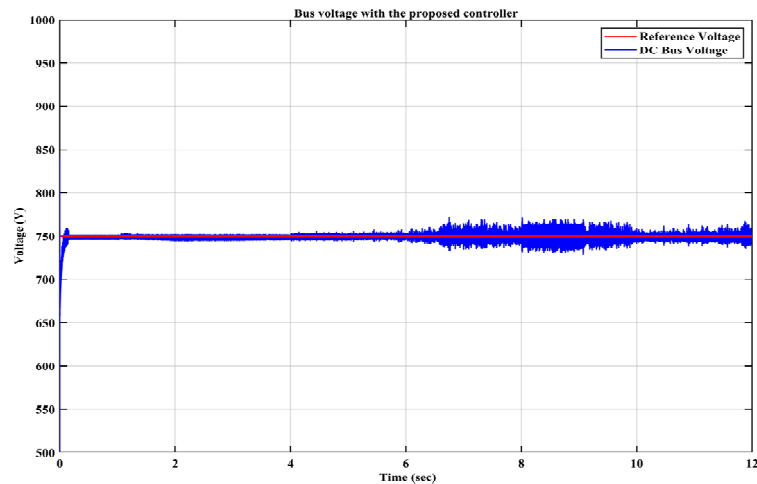


Figure 14. DC bus voltage with the proposed controller.

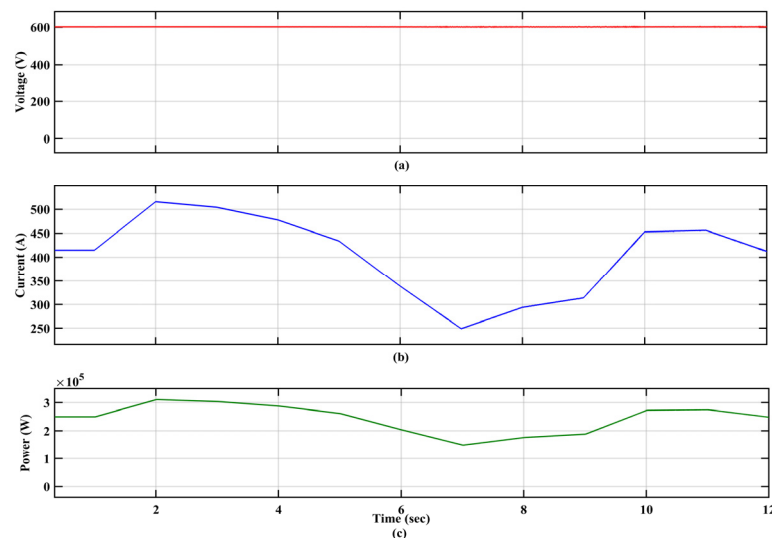


Figure 15. Solar PV (a) voltage, (b) current, and (c) power with the proposed controller.

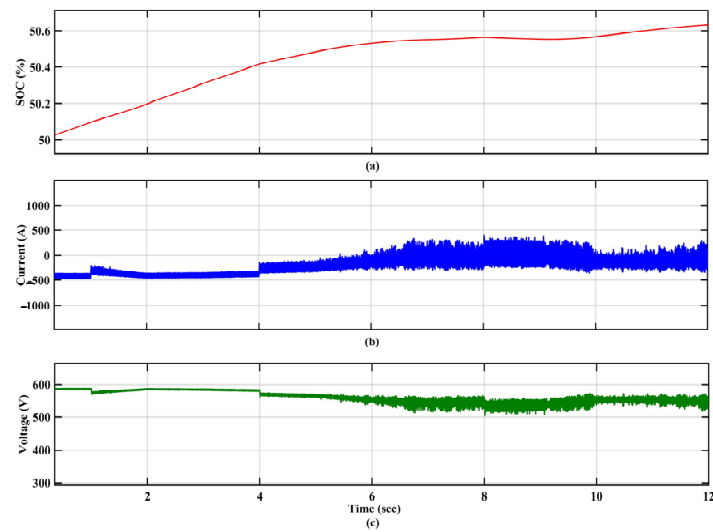


Figure 16. ESU (a) SOC, (b) current, and (c) voltage with the proposed controller.

#### 4.2.2. Region II ( $t = 4$ to $t = 8$ s)

EV<sub>2</sub> is plugged into the charging station at  $t = 4$  sec and EV<sub>1</sub> is plugged in throughout the simulation time, which increases the load current to 250 A. This means that the charging station is under two-thirds load. The load current now falls into  $R_{II}$ , which is less than  $I_{r2}$  and greater than  $I_{r1}$ . The control algorithm now calculates  $p_1$  and updates the droop value and compensates for the reference voltage. The maximum real-time solar irradiation obtained in this region is  $626 \text{ W/m}^2$ . The bus voltage with the proposed controller is tracking the reference voltage more accurately when compared to the bus voltage with the MPPT controller. The fluctuations in the bus voltage at  $t = 4$  s settle down in 0.12 s. Also, the ripples in the ESU current are very much reduced with the proposed controller when compared to the MPPT controller, which is evident from Figure 16. With this, the power balance is also improved with the proposed controller when compared to the MPPT controller in  $R_{II}$  as shown in Figure 17. At  $t = 7$  s, the solar irradiation is at its lowest value, which is  $304 \text{ W/m}^2$ , and the power produced by the solar PV is sufficient to supply the load to the bus, but the rate of charge of the ESU battery slows down at this instance.

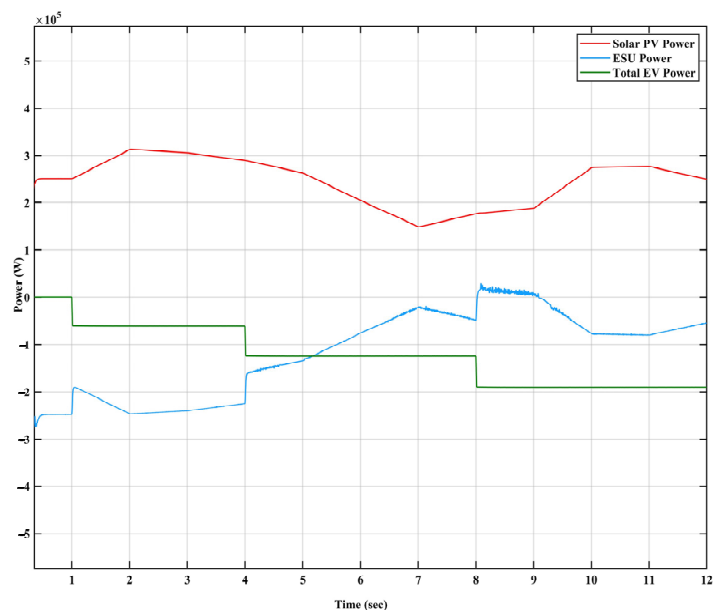


Figure 17. Power sharing with the proposed controller.

#### 4.2.3. Region III ( $t = 8$ to $t = 12$ s)

EV<sub>3</sub> is plugged into the charging station at  $t = 8$  s. The charging station is under full load. The EV load current is 375 A, which falls into  $R_{III}$  of the piece-wise droop curve. The proposed control algorithm calculates and updates the droop value of  $R_{III}$  and the voltage compensation to achieve less voltage regulation and proper power balance. The fluctuations in the bus voltage at  $t = 8$  s after connecting EV<sub>3</sub> rise to 771.45 V and die out within 0.9 s, reverting back to the reference voltage. The solar PV power is not enough to supply the full load with its variable irradiation at the instance of  $t = 7$ , and the ESU changes to boost mode to deliver the load for about a second and then switches back to buck mode since the irradiation continues generating solar PV power sufficient to charge the EV load.

Figure 18 represents the voltage, current, and SOC level of EV<sub>1</sub>. Similarly, Figure 19 is for EV<sub>2</sub> and Figure 20 is for EV<sub>3</sub> throughout the operation. EV<sub>1</sub> charges from 30% SOC to 30.34% in 12 s from  $t = 1$  to  $t = 12$  s. EV<sub>2</sub> charges from the initial SOC of 30% at  $t = 4$  s to 30.25% at  $t = 12$  s. EV<sub>3</sub> charges from 30% SOC at  $t = 8$  s to 30.13% at  $t = 12$  s.

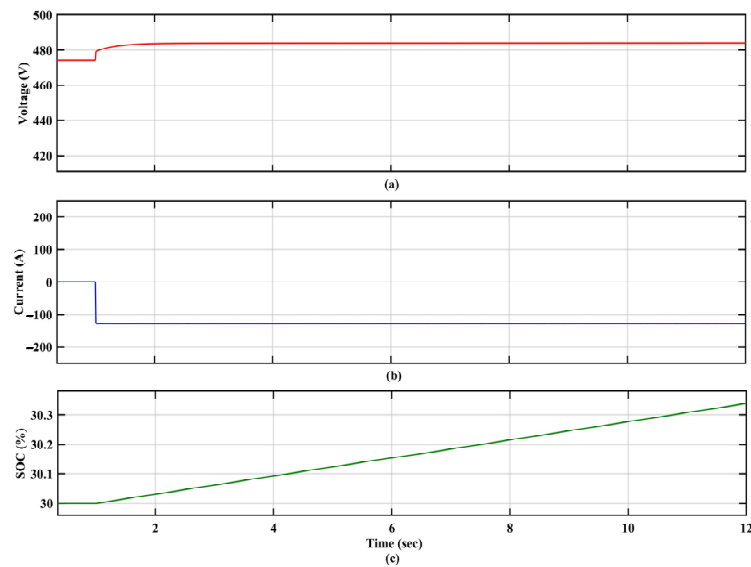


Figure 18. EV<sub>1</sub> (a) voltage, (b) current, and (c) SOC with the proposed controller.

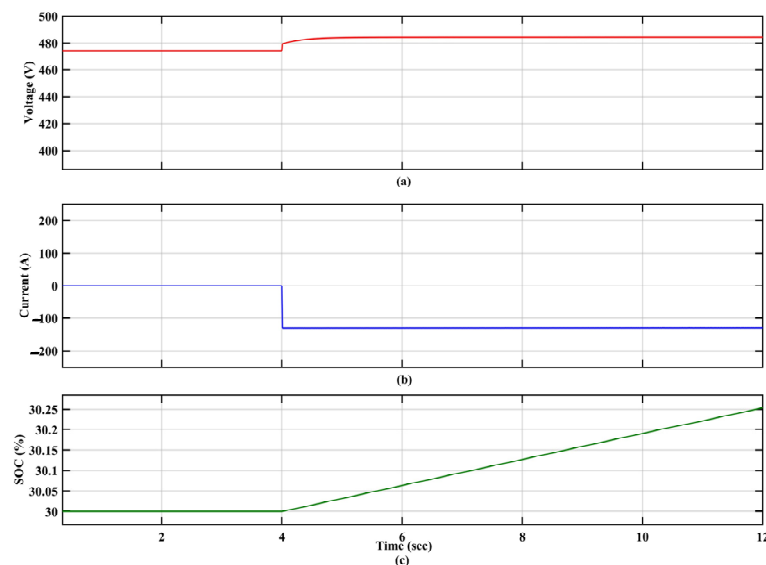
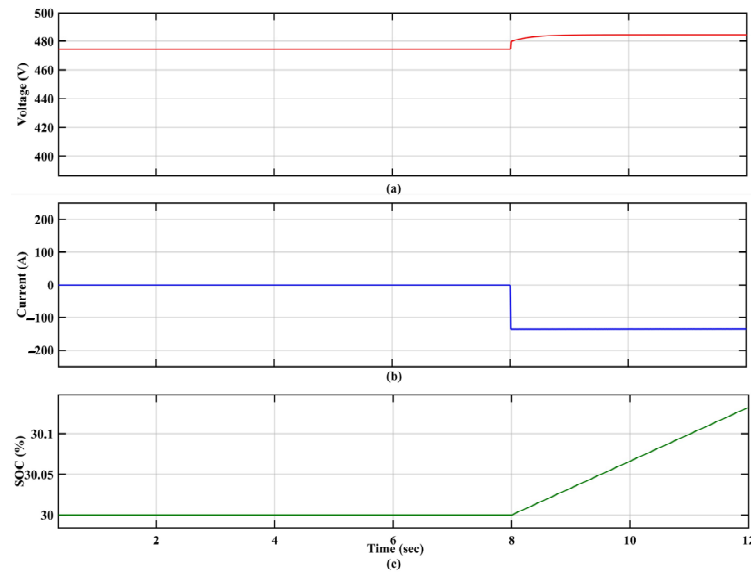


Figure 19. EV<sub>2</sub> (a) voltage, (b) current, and (c) SOC with the proposed controller.



**Figure 20.** EV<sub>3</sub> (a) voltage, (b) current, and (c) SOC with the proposed controller.

The fast-charging criteria are fulfilled by charging the SOC up to 80% within an hour. Each EV is charging at a rate of 500 V and 125 A with a 62.5 kW fast charger. Table 4 shows the performance analysis of FEVCS with the widely used MPPT controller and the proposed piece-wise droop controller, proving the superiority of the proposed controller in attaining proper voltage regulation and improved dynamic performance. The improvement in the power balance between various sources with the proposed controller is evident from comparing Figures 1 and 17. The periodic voltage of the DC bus, solar PV, and ESU with the proposed controller is listed in Appendix C, Table A4.

**Table 4.** Qualitative comparative analysis of MPPT and the proposed controller.

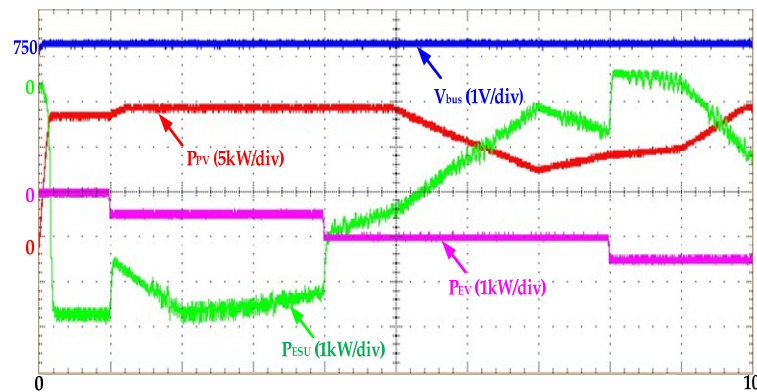
| Performance Index             | Controller       | $R_I$<br>(1–4 s) | $R_{II}$<br>(4–8 s) | $R_{III}$<br>(8–12 s) |
|-------------------------------|------------------|------------------|---------------------|-----------------------|
| Maximum voltage deviation (%) | MPPT             | 12.16            | 12.91               | 12.66                 |
|                               | Piece-wise droop | 0.57             | 2.89                | 2.82                  |
| Settling time ( $t_s$ ) (s)   | MPPT             | 0.14             | 0.30                | 1.45                  |
|                               | Piece-wise droop | 0.07             | 0.12                | 0.9                   |

## 5. Experimental Validation in RT Lab

The effectiveness of FEVCS using the proposed piece-wise droop controller has been validated in the RT lab using the OP4500 OPAL-RT real-time digital simulator (RTDS), which replicates real-time conditions. FEVCS is simulated for 10 s in RTDS with the proposed controller with three regions for real-time variable solar irradiation and dynamic EV load. The Simulink model undergoes compilation by the host PC via the RT-LAB interface. The outcomes are captured utilizing a digital storage oscilloscope (DSO) via the analog outputs of the OP4500 target. To check the similarity of the proposed FEVCS with the simulation results, a sampling time of 30  $\mu$ s is considered to obtain HIL results in RT lab.

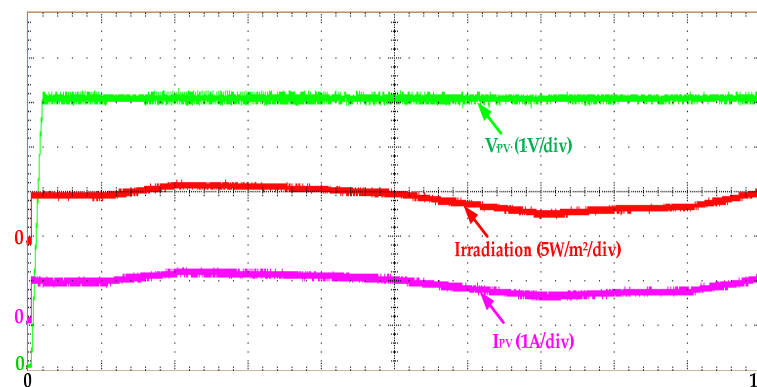
Figure 21 represents the real-time results of the DC bus voltage and power sharing between the solar PV and ESU for a variable EV load with the proposed piece-wise droop controller, which is in complete agreement with Figures 14 and 17 for all the three regions of the proposed piece-wise droop controller, i.e.,  $R_I$ ,  $R_{II}$ , and  $R_{III}$ . The solar PV and ESU are sharing power according to the change in EV load. The bus voltage is almost tracing the reference voltage of 750 V, which shows the robustness of the proposed controller in

maintaining bus stability. The EV load changes at the time instants of  $t = 1$ , i.e.,  $R_I$ ,  $t = 4$ , i.e.,  $R_{II}$  and  $t = 8$  s, i.e.,  $R_{III}$ . At  $t = 4.1$  s, i.e., in  $R_{II}$ , the total solar PV power is 285 kW, which is supplying 125 kW of the EV load, and the balanced power is charging the ESU battery, which is approximately 160 kW. The appropriate power sharing of the sources along with the stable bus voltage is possible due to the droop updating in individual regions of the proposed three-region piece-wise droop controller.



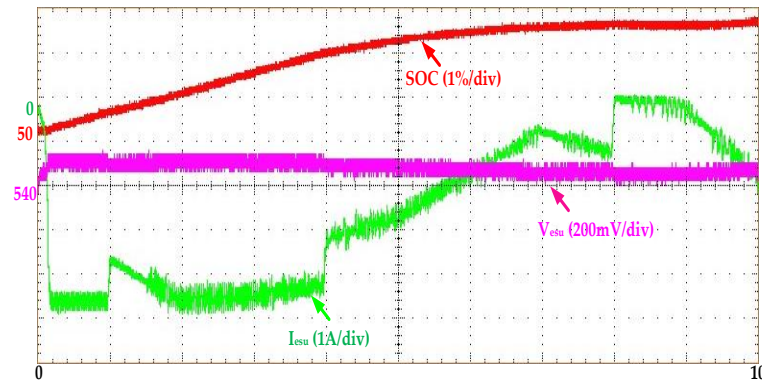
**Figure 21.** RT lab results for bus voltage and power sharing of FEVCS with the proposed controller.

Figure 22 represents the variable solar irradiation and voltage and current of solar PV with the proposed piece-wise droop controller integrated with voltage compensation using the OPAL-RT digital simulator. The voltage of the solar PV is almost constant at 600 V throughout the operation, irrespective of the variable irradiation and EV dynamics, showcasing the effectiveness of the proposed controller. The solar current follows the variable irradiation, which is in complete agreement with the simulation plot shown in Figure 15.



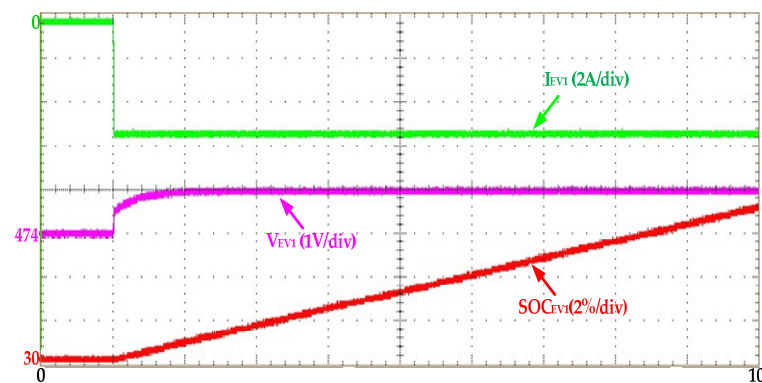
**Figure 22.** RT lab results for solar PV input irradiation, voltage, and current of FEVCS with the proposed controller.

Figure 23 shows the RT lab results of the ESU SOC, voltage, and current with the proposed controller. Whenever the ESU is charging, the SOC of the ESU is raised, and when the ESU is discharging, the SOC falls. The rate of rise and fall of the SOC of the ESU depends on the charging and discharging current, which in turn is determined by the EV load dynamics and the solar irradiation. This plot confirms that the ESU is operating bidirectionally, which is desirable and crucial for the stable operation of FEVCS. The initial SOC of the ESU is 50% and is charged to 50.57% until  $t = 8$  s due to the sufficient power supplied from the solar PV to meet the EV load demand and to charge the ESU. At  $t = 8$  s, the solar PV power is insufficient to supply the EV load, and the SOC of the ESU starts discharging from 50.57% to 50.56% until  $t = 8.5$  s to facilitate a balanced EV load demand. The ESU voltage drops from 545.5 V at  $t = 8$  s to 523 V at  $t = 8.5$  s.



**Figure 23.** RT lab results for ESU SOC, voltage, and current of FEVCS with the proposed controller.

Figures 24–26 depict the real-time results of the SOC, voltage, and current of EV<sub>1</sub>, EV<sub>2</sub>, and EV<sub>3</sub>, respectively, with the proposed piece-wise droop controller. The initial SOC of all the EVs is considered to be 30%, and the EVs are charging at 125 A with 62.5 kW rapid chargers. The initial voltage of the EVs is 474 V. The voltage and SOC keep rising throughout the time the EVs are connected to the DC fast chargers. These results are in complete agreement with the simulation results of the EVs, which are depicted in Figures 18–20 from the previous section. The SOC of EV<sub>1</sub> rises from 30% at  $t = 1$  s to 30.28% at  $t = 10$  s. Similarly, EV<sub>2</sub> rises from 30% at  $t = 4$  s to 30.19% at  $t = 10$  s and EV<sub>3</sub> rises from 30% at  $t = 8$  s to 30.07% at  $t = 10$  s. Based on this analysis, it is evident that reaching 80% state of charge (SOC) for the EV battery takes less than an hour, showcasing the fast charging capabilities of the proposed FEVCS with the piece-wise droop controller.



**Figure 24.** RT lab results for EV<sub>1</sub> SOC, voltage, and current with the proposed controller.

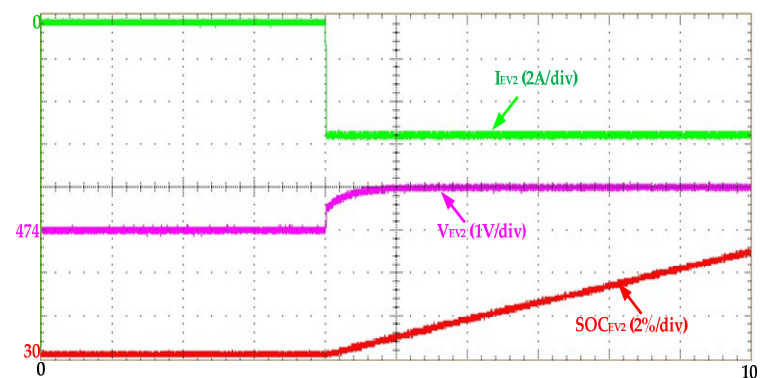


**Figure 25.** RT lab results for EV<sub>2</sub> SOC, voltage, and current with the proposed controller.

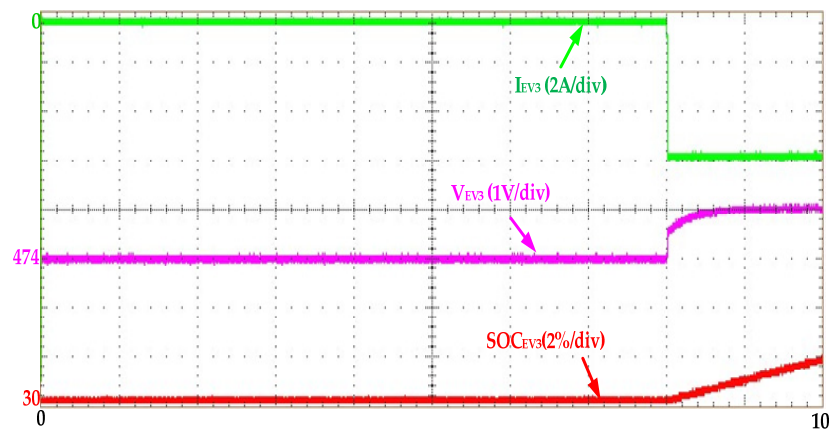


**Figure 26.** RT lab results for EV<sub>3</sub> SOC, voltage, and current with the proposed controller.

Table 5 discusses the comparison of existing work in the literature with the proposed FEVCS model using a piece-wise droop controller in this work. This indicates the effectiveness of the proposed piece-wise droop controller in achieving proper power sharing and minimal voltage deviation with an intermittent source and load.

**Table 5.** Comparison of performance of existing literature with the proposed droop controller.

|                        | Ref [22] | Ref [23] | Ref [24] | Ref [25] | Ref [29] | Proposed FEVCS |
|------------------------|----------|----------|----------|----------|----------|----------------|
| Voltage level (V)      | 48       | 6 k      | 380      | 750      | 10       | 750            |
| Dynamic input          | ✓        | ✗        | ✗        | ✗        | ✗        | ✓              |
| Dynamic EV load        | ✗        | ✗        | ✗        | ✓        | ✗        | ✓              |
| Fast charging          | ✗        | ✗        | ✗        | ✓        | ✗        | ✓              |
| Proper power sharing   | ✓        | ✓        | ✓        | ✓        | ✓        | ✓              |
| Voltage regulation (%) | 1.29     | 1.72     | 0.70     | 5.00     | 4.50     | 0.84           |

✗—Not considered; ✓—Considered.

## 6. Conclusions

A piece-wise droop controller with three regions is proposed for a microgrid-based DC fast EV charging station integrated with a solar PV, ESU, and EV load consisting of three 62.5 kW fast chargers. An evaluation of the dynamic performance of the system is conducted under intermittent source and load conditions, comparing the traditional MPPT controller with the proposed piece-wise droop controller.

Unlike the traditional droop controller, the voltage regulation and power balance are improved with the proposed controller without any trade-off. The relative comparison between MPPT control and the proposed control strategy for one-third, two-thirds, and full load conditions reveals that the proposed piece-wise droop controller has achieved 7.48%, 10.02%, and 9.84% improved voltage regulation, respectively. Also, a further observation infers that the settling time of the proposed controller for Region I is 0.07 s, whereas the MPPT's settling time is 0.14 s, which is double the time required by the proposed controller. Similarly, for the second and third regions, the proposed controller leads the MPPT controller by 0.18 s and 0.1 s, respectively. Mapping the settling time of the controller with respective voltage fluctuation against the EV dynamics at various load conditions, it is inferred that the proposed piece-wise droop controller has achieved improved dynamic stability compared to the MPPT controller. The HIL results and modeling findings have corroborated the bus voltage stability and dynamic stability during the rapid charging of EVs under intermittent source and load conditions. This study concludes that the proposed controller for the DC-microgrid-based FEVCS offers significant benefits in remote areas

with unreliable or nonexistent power grids, thereby enhancing reliability and sustainability in the clean transportation sector.

**Author Contributions:** M.M.: Conceptualization, Methodology, Software, Validation, Formal Analysis, Investigation, Writing—original draft. B.A.R.: Supervision, Resources, Methodology, Conceptualization, Investigation, Writing—review & editing. M.L.K.: Supervision, Methodology, Conceptualization, Investigation, Formal Analysis, Writing—review & editing. K.R.N.: Supervision, Investigation, Formal Analysis, Writing—review & editing. J.R.M.: Formal Analysis, Writing—review & editing. S.K.K.: Formal Analysis, Writing—review & editing. All authors have read and agreed to the published version of the manuscript.

**Funding:** This research received no external funding.

**Data Availability Statement:** The original contributions presented in the study are included in the article, further inquiries can be directed to the corresponding author.

**Conflicts of Interest:** The authors declare no conflicts of interest.

## Appendix A

**Table A1.** System design parameters.

|                                 |   |                |
|---------------------------------|---|----------------|
| Solar PV array                  | Number of cells                               | $98 \times 17$ |
|                                 | Open circuit voltage per module ( $I_{sc}$ )  | 44.4 V         |
|                                 | Short circuit current per module ( $V_{oc}$ ) | 8.69 A         |
|                                 | Maximum power per module ( $P_{mpp}$ )        | 300.12 W       |
|                                 | Maximum input voltage ( $V_{pv-max}$ )        | 622.2 V        |
|                                 | Maximum solar PV current ( $I_{mpp}$ )        | 803.6 A        |
|                                 | Maximum solar PV power ( $P_{pv-mpp}$ )       | 500 kW         |
| Uni-directional DC-DC converter | $L_{pv}$                                      | 0.0463 mH      |
|                                 | $C_{out}$                                     | 16.11 $\mu$ F  |
|                                 | $C_{pv}$                                      | 0.1 F          |
|                                 | $R_{cp}$                                      | 0.005 $\Omega$ |
|                                 | $V_{ref}$                                     | 750 V          |
|                                 | Switching frequency                           | 20 kHz         |
|                                 | $R_{in}$                                      | 0.05 $\Omega$  |
| Piece-wise droop controller     | PI controller gains                           | 0.9, 0.0015    |
|                                 | $I_{r1}, I_{r2}$                              | 150 A, 300 A   |
| ESU                             | $a, b$  | 1, 1           |
|                                 | $V_{esu}$                                     | 500 V          |
|                                 | Capacity                                      | 100 Ah         |
| Bi-directional DC-DC converter  | Initial SOC                                   | 50%            |
|                                 | $L_{esu}$                                     | 92.5 $\mu$ H   |
|                                 | $C_{esu}$                                     | 1 mF           |
|                                 | $R_{ce}$                                      | 0.006 $\Omega$ |
| EV battery                      | PI controller gains                           | 0.002, 0.068   |
|                                 | $V_{ev}$                                      | 444 V          |
|                                 | Capacity                                      | 114 Ah         |
|                                 | Initial SOC                                   | 30%            |

**Table A1.** Cont.

|                 |                     |                       |
|-----------------|---------------------|-----------------------|
| EV fast Charger | Rating              | 62.5 kW, 500 V, 125 A |
|                 | $L_{ev}$            | 20 mH                 |
|                 | $C_{ev}$            | 25 $\mu$ F            |
|                 | PI controller gains | 0.75, 50              |

## Appendix B

**Table A2.** Piece-wise droop value calculation.

| Parameter    | Calculation   | Value  |
|--------------|---|--------|
| $\delta V_1$ | $\frac{37.5}{1+1\left(\left(\frac{3}{2}(3+1)\right)-1\right)}$                        | 6.25   |
| $\delta I_3$ | $\frac{515.5}{1+1\left(\left(\frac{3}{2}(3+1)\right)-1\right)}$                       | 85.92  |
| $d_{11}$     | $\left(\frac{1}{1}\right)\left(\frac{2}{3+1-2}\right)\left(\frac{6.25}{85.92}\right)$ | 0.0727 |
| $d_{111}$    | $\left(\frac{1}{1}\right)\left(\frac{3}{3+1-3}\right)\left(\frac{6.25}{85.92}\right)$ | 0.2182 |

**Table A3.** Compensation in reference value calculation.

| Parameter         | Calculation   | Value |
|-------------------|---|-------|
| $\delta V_{ref1}$ | $\left(\frac{150+300}{2}\right) \times 0.05 \times 1$ | 11.25 |
| $\delta V_{ref2}$ | $\left(\frac{150+300}{2}\right) \times 0.05 \times 2$ | 22.5  |

## Appendix C

**Table A4.** Periodic variations of  $V_{bus}$  with the proposed piece-wise droop controller.

| Time (s)                        | 0.5   | 2     | 3     | 5     | 6     | 7     | 9     | 10    | 11    |
|---------------------------------|-------|-------|-------|-------|-------|-------|-------|-------|-------|
| Irradiation (W/m <sup>2</sup> ) | 504   | 626   | 612   | 527   | 412   | 304   | 382   | 550   | 554   |
| $V_{pv}$ (V)                    | 601.5 | 601.8 | 601.7 | 601.6 | 601.3 | 600.6 | 601.1 | 601.6 | 601.5 |
| $V_{esu}$ (V)                   | 586   | 585.1 | 584   | 564.2 | 552.5 | 540.2 | 534.6 | 551.5 | 554.6 |
| $V_{bus}$ (V)                   | 751   | 751.4 | 748.3 | 749.7 | 749.9 | 735.7 | 752.7 | 756.3 | 750.2 |

## References

- Jawale, S.A.; Singh, S.K.; Singh, P.; Kolhe, M.L. Priority wise electric vehicle charging for grid load minimization. *Processes* **2022**, *10*, 1898. [CrossRef]
- Gržanić, M.; Hrga, A.; Capuder, T. Profitable Investment in PV and BES Integrated with EV Charging Stations in Croatia—Myth or Reality? In Proceedings of the 2022 7th International Conference on Smart and Sustainable Technologies (SpliTech), Split/Bol, Croatia, 5–8 July 2022; IEEE: Piscataway, NJ, USA, 2022; pp. 1–6.
- Bilal, M.; Ahmad, F.; Rizwan, M. Techno-economic assessment of grid and renewable powered electric vehicle charging stations in India using a modified metaheuristic technique. *Energy Convers. Manag.* **2023**, *284*, 116995. [CrossRef]
- Bragatto, T.; Bucarelli, M.A.; Carere, F.; Santori, F. Transition to Electric Vehicles in a Company's fleet: Design and Policy on a Case Study. In Proceedings of the 2022 7th International Conference on Smart and Sustainable Technologies (SpliTech), Split/Bol, Croatia, 5–8 July 2022; IEEE: Piscataway, NJ, USA, 2022; pp. 1–6.
- Wu, Y.; Wang, Z.; Huangfu, Y.; Ravey, A.; Chrenko, D.; Gao, F. Hierarchical operation of electric vehicle charging station in smart grid integration applications—An overview. *Int. J. Electr. Power Energy Syst.* **2022**, *139*, 108005. [CrossRef]
- Lou, G.; Hong, Y.; Li, S. Distributed secondary voltage control for DC microgrids with consideration of asynchronous sampling. *Processes* **2021**, *9*, 1992. [CrossRef]

7. Nasir, M.; Iqbal, S.; Khan, H.A.; Vasquez, J.C.; Guerrero, J.M. Sustainable rural electrification through solar PV DC microgrids—An architecture-based assessment. *Processes* **2020**, *8*, 1417. [[CrossRef](#)]
8. Inci, M.; Çelik, Ö.; Lashab, A.; Bayındır, K.Ç.; Vasquez, J.C.; Guerrero, J.M. Power System Integration of Electric Vehicles: A Review on Impacts and Contributions to the Smart Grid. *Appl. Sci.* **2024**, *14*, 2246. [[CrossRef](#)]
9. Arya, H.; Das, M. Fast charging station for electric vehicles based on DC microgrid. *IEEE J. Emerg. Sel. Top. Ind. Electron.* **2023**, *4*, 1204–1212. [[CrossRef](#)]
10. Aluisio, B.; Bruno, S.; De Bellis, L.; Dicorato, M.; Forte, G.; Trovato, M. DC-microgrid operation planning for an electric vehicle supply infrastructure. *Appl. Sci.* **2019**, *9*, 2687. [[CrossRef](#)]
11. Naik, K.R.; Rajpathak, B.; Mitra, A.; Sadanala, C.; Kolhe, M.L. Power management scheme of DC micro-grid integrated with photovoltaic-Battery-Micro hydro power plant. *J. Power Sources* **2022**, *525*, 230988. [[CrossRef](#)]
12. Ko, H.; Kim, G.; Nam, Y.; Ryu, K. Supervisory Power Coordination Scheme to Mitigate Power Curtailment in the Application of a Microgrid. *Processes* **2021**, *9*, 1998. [[CrossRef](#)]
13. Yadav, A.K.; Bharatee, A.; Ray, P.K. Solar-powered grid integrated charging station with hybrid energy storage system. *J. Power Sources* **2023**, *582*, 233545. [[CrossRef](#)]
14. Dubravac, M.; Šimić, Z.; Topić, D.; Knežević, G.; Fekete, K. Analysis of PV and EV Chargers Integration Impact on Radial LV Distribution Network. In Proceedings of the 2023 8th International Conference on Smart and Sustainable Technologies (SpliTech), Split/Bol, Croatia, 20–23 June 2023; IEEE: Piscataway, NJ, USA, 2023; pp. 1–5.
15. Li, M.; Fan, J.; Qiao, L. Adaptive droop control of a multibus DC microgrid based on consensus algorithm. *Math. Probl. Eng.* **2021**, *2021*, 6634278. [[CrossRef](#)]
16. Taye, B.A.; Choudhury, N.B.D. A dynamic droop control for a DC microgrid to enhance voltage profile and proportional current sharing. *Electr. Power Syst. Res.* **2023**, *221*, 109438. [[CrossRef](#)]
17. Shebani, M.M.; Iqbal, T.; Quaicoe, J. Comparison between alternative droop control strategy, modified droop method and control algorithm technique for parallel-connected converters. *AIMS Electron. Electr. Eng.* **2021**, *5*, 1–23. [[CrossRef](#)]
18. Li, D.; Zhao, D. An Improved Distributed Secondary Control to Attain Concomitant Accurate Current Sharing and Voltage Restoration in DC Microgrids. In Proceedings of the 2021 40th Chinese Control Conference (CCC), Shanghai, China, 26–28 July 2021; IEEE: Piscataway, NJ, USA, 2021; pp. 3834–3839.
19. Prabhakaran, P.; Goyal, Y.; Agarwal, V. A novel communication-based average voltage regulation scheme for a droop controlled DC microgrid. *IEEE Trans. Smart Grid* **2017**, *10*, 1250–1258. [[CrossRef](#)]
20. Mesbah, M.A.; Sayed, K.; Ahmed, A.; Aref, M.; Elbarbary, Z.M.S.; Almuflih, A.S.; Mossa, M.A. Adaptive Control Approach for Accurate Current Sharing and Voltage Regulation in DC Microgrid Applications. *Energies* **2024**, *17*, 284. [[CrossRef](#)]
21. Hosseinipour, A.; Khazaei, J. A multifunctional complex droop control scheme for dynamic power management in hybrid DC microgrids. *Int. J. Electr. Power Energy Syst.* **2023**, *152*, 109224. [[CrossRef](#)]
22. Huang, H.; Balasubramaniam, S.; Todeschini, G.; Santoso, S. A photovoltaic-fed dc-bus islanded electric vehicle charging system based on a hybrid control scheme. *Electronics* **2021**, *10*, 1142. [[CrossRef](#)]
23. Naik, K.R.; Rajpathak, B.; Mitra, A.; Kolhe, M. Renewable Energy Integrated DC Microgrid for EV Charging Station. In Proceedings of the 2021 IEEE Transportation Electrification Conference (ITEC-India), New Delhi, India, 16–19 December 2021; IEEE: Piscataway, NJ, USA, 2022; pp. 1–6.
24. Naik, K.R.; Kolhe, M.; Prasad, M.K.S. Predictive Control Strategy for DC Microgrid Integrated EV Charging Stations in Oslo. In Proceedings of the 2024 4th IEEE Sustainable Energy and Future Electric Transportation (SEFET-India), Hyderabad, India, 31 July–3 August 2024; IEEE: Piscataway, NJ, USA, 2024. *accepted*.
25. Liu, S.; Zheng, J.; Li, Z.; Li, R.; Fang, W.; Liu, X. Distributed Piecewise Droop Control of DC Microgrid with Improved Load Sharing and Voltage Compensation. In Proceedings of the 2019 IEEE Third International Conference on DC Microgrids (ICDCM), Matsue, Japan, 20–23 May 2019; IEEE: Piscataway, NJ, USA, 2020; pp. 1–6.
26. D’Arco, S.; Suul, J.A. Generalized implementations of piecewise linear control characteristics for multiterminal HVDC. In Proceedings of the 2014 International Symposium on Power Electronics, Electrical Drives, Automation and Motion, Ischia, Italy, 18–20 June 2014; IEEE: Piscataway, NJ, USA, 2014; pp. 66–72.
27. Hailu, T.; Ferreira, J.A. Piece-wise linear droop control for load sharing in low voltage DC distribution grid. In Proceedings of the 2017 IEEE Southern Power Electronics Conference (SPEC), Puerto Varas, Chile, 4–7 December 2017; IEEE: Piscataway, NJ, USA, 2018; pp. 1–6.
28. Lin, Y.; Xiao, W. Novel piecewise linear formation of droop strategy for DC microgrid. *IEEE Trans. Smart Grid* **2019**, *10*, 6747–6755. [[CrossRef](#)]
29. Sharma, S.; Iyer, V.M.; Bhattacharya, S. A load profile-based optimized piecewise droop control for DC microgrids. In Proceedings of the 2021 IEEE Fourth International Conference on DC Microgrids (ICDCM), Arlington, VA, USA, 18–21 July 2021; IEEE: Piscataway, NJ, USA, 2021; pp. 1–7.

**Disclaimer/Publisher’s Note:** The statements, opinions and data contained in all publications are solely those of the individual author(s) and contributor(s) and not of MDPI and/or the editor(s). MDPI and/or the editor(s) disclaim responsibility for any injury to people or property resulting from any ideas, methods, instructions or products referred to in the content.